International Journal of Applied Earth Observations and Geoinformation 114 (2022) 103056

Contents lists available at ScienceDirect

International Journal of Applied Earth Observation and Geoinformation

journal homepage: www.elsevier.com/locate/jag

Peering through the thicket: Effects of UAV LiDAR scanner settings and flight planning on canopy volume discovery

Benjamin Brede [a,b,*], Harm M. Bartholomeus [b], Nicolas Barbier [c], François Pimont [d], Grégoire Vincent [c], Martin Herold [a,b]

[a] Helmholtz Center Potsdam GFZ German Research Centre for Geosciences, Section 1.4 Remote Sensing and Geoinformatics, Telegrafenberg, 14473 Potsdam, Germany
[b] Wageningen University & Research, Laboratory of Geo-Information Science and Remote Sensing, Droevendaalsesteeg 3, 6708 PB Wageningen, The Netherlands
[c] AMAP, University Montpellier, IRD, CNRS, CIRAD, INRAE, Montpellier, France
[d] INRAE UR629, UR Ecologie des Forêts Méditerranéennes, INRA, Avignon, France

ARTICLE INFO

Keywords:
Unoccupied aerial vehicle laser scanning (UAV-LS)
Occlusion
Forest structure

ABSTRACT

Unoccupied aerial vehicle laser scanning (UAV-LS) has been increasingly used for forest structure assessment in recent years due to the potential to directly estimate individual tree attributes and availability of commercial solutions. However, standardised procedures for campaign planning are still largely missing. This study investigated scanner properties and flight planning to provide recommendations on minimising forest canopy occlusion and thereby maximise exploration of canopy volume. A flight campaign involving two UAV-LS systems was conducted over a dense, wet tropical forest at the Paracou research station (French Guiana). Four experiments on scanner properties and flight planning were conducted, analysed and recommendations derived. First, the scanner pulse repetition rate (PRR) should be at least 100 kHz per 1 m s^{-1} flight speed based on 360° FOV for exploration of middle canopy strata (5 m to 20 m). Higher PRR are beneficial for exploration of lower canopy (<5 m) but would need to be increased exponentially to achieve linear improvement. Alternatively, flight speed could be reduced within the constraints given by the inertial measurement unit (IMU), but would increase flight time. Second, the scanner maximum range was identified as a proxy for the laser pulse power, which positively impacts canopy exploration. This was particularly the case when using multi-return capabilities. No saturation could be observed when increasing the laser power, suggesting that this is currently a limiting factor. Additionally, a smaller laser beam divergence and pulse width were plausible reasons for better exploration of the upper canopy just below the top of canopy. Third, off-nadir scanning angles up to 20° were found to result in similar occlusions, suggesting a practical FOV of 40° in the investigated dense forest. This number might be larger for open canopies. UAV-LS systems with viewing geometries that focus laser pulses downwards and within optimal ranges should be preferred. Fourth, using different horizontal flight directions in the mission planning favours minimisation of occlusion. A minimum of two different flight directions is suggested. However, specific optimal yaw angles were not possible to predict before flight. Therefore, including multiple directions ensures coverage of all possible configurations. Many of these investigated features can be optimised independently from each other, and should be considered before acquisition of new UAV-LS systems and flight mission planning. These results support the establishment of general guidelines for the investment in UAV-LS systems and optimal mission planning for forest structure assessment.

1. Introduction

In recent years, unoccupied aerial vehicle laser scanning (UAV-LS) have been increasingly used for vegetation and in particular forest structure assessment (Wallace et al., 2012; Mandlburger et al., 2015; Kellner et al., 2019; Terryn et al., 2022). They have the advantage of collecting high-density points clouds (≫100 points/m^2), thereby bridging the gap between terrestrial laser scanning (TLS) and airborne laser scanning (ALS). Potential metrics that can be estimated cover on the one hand discrete geometrical metrics that measure individual tree dimensions like diameter at breast height (DBH), height and crown

* Corresponding author at: Helmholtz Center Potsdam GFZ German Research Centre for Geosciences, Section 1.4 Remote Sensing and Geoinformatics, Telegrafenberg, 14473 Potsdam, Germany.
E-mail address: benjamin.brede@gfz-potsdam.de (B. Brede).

https://doi.org/10.1016/j.jag.2022.103056
Received 22 April 2022; Received in revised form 7 October 2022; Accepted 10 October 2022
Available online 1 November 2022

metrics (Wallace et al., 2014a; Brede et al., 2017), and on the other hand foliage and vegetation density (Jupp et al., 2009; Calders et al., 2015; Pimont et al., 2018; Schneider et al., 2019). All metrics' estimation procedures depend on the properties of the UAV-LS including point density and ability of the laser to explore all vegetation layers.

In the context of canopy exploration, the concept of occlusion is commonly applied. The degree of occlusion will determine the amount of volume explored. Occlusion is the blocking effect of the laser pulse by vegetation elements that effectively prevents the exploration of canopy volume. It has direct consequences for the estimation of canopy and individual tree properties. For example, occlusion typically prevents reliable DBH estimation with UAV-LS (Brede et al., 2017; Levick et al., 2021; Vandendaele et al., 2021; Terryn et al., 2022). Occlusion also induces biases in leaf area density (LAD) estimation and these biases can be heterogeneously distributed in the canopy (Soma et al., 2021), because dense regions in the canopy have the tendency to be less explored. Occlusion is a direct consequence of UAV-LS system properties and sampling strategy, i.e. the arrangement of flight lines.

Countermeasures to overcome occlusion depend on the system and task at hand. In TLS, a multi-view point sampling strategy was recommended to maximise canopy exploration (Wilkes et al., 2021). UAV-LS and ALS have the advantage of being mounted on moving platforms, thereby increasing the number of viewpoints as compared to TLS and potentially increasing canopy exploration. However, the upper canopy has a strong shielding effect that inhibits discovery of understorey (Brede et al., 2017), which has a negative influence not only on foliage density estimation, but also on stem and branch discovery required for forest inventories and above-ground biomass (AGB) estimation (Wieser et al., 2017; Brede et al., 2017, 2019, 2022; Wallace et al., 2014a,b). A very effective strategy would be to fly below the canopy. For example, Hyyppä et al. (2020) implemented a UAV-LS that could be operated below-canopy via video goggles in two boreal forest plots. While this approach could support forest inventories in sparse forests, technological advancements in the field of autonomous unoccupied aerial vehicle (UAV) navigation and collision avoidance of small branches and lianas are required to make this technique applicable in dense forests. Kükenbrink et al. (2017) investigated occlusion in ALS data over forests and found that increased flight line overlap leads to increased angular sampling and pulse density on the canopy, and can counteract occlusion. Schneider et al. (2019) combined TLS and UAV-LS to reduce occlusion to <2 % considering a voxel size of 10 cm. In addition to decisions on these flight and scan patterns, an increasing number of UAV-LS scanners are available on the commercial market, including downward looking, or wide-angle systems, or systems with different multi-return capabilities. Also, different light detection and ranging (LiDAR) range capabilities are available. The wealth of options requires systematic investigations as to which system properties and scanning setups should be favoured for the tasks at hand.

The aim of this study was to identify the impact of selected scanner settings and properties, and flight planning on canopy exploration by laser beams, thanks to four sensitivity experiments. The investigated scanner properties were pulse repetition rate (PRR), laser power and wavelength, and scanning angle, while the addition of flight lines to the flight plan was considered for flight planning options. The analysis was based on a data set collected by two UAV-LS systems over a dense tropical forest. The findings aim to support researchers and flight operators in the decision on desirable scanner properties and flight setups, as well as laying the basis for general recommendations and further standardisation of UAV-LS operations, comparable to what has been achieved for TLS (e.g., by Wilkes et al. 2017).

2. Data and methods

2.1. Study site

The data for this study were collected at plot 6 of the Paracou Research Station in French Guiana (N5°18′ W52°53′, https://paracou.cirad.fr/). The forests of Paracou are lowland tropical forests of the Guiana Shield and as such characterised by complex structure with multiple canopy layers. Among the 16 plots of Paracou, plot 6 was the one with the highest AGB density with 421.9 Mg ha^{-1} according to 2017 census data. The canopy reaches on average heights of 27.2 m with top heights up to 44.8 m (Fig. 1).

2.2. UAV-LS systems and data collection

A field campaign was conducted with two UAV-LS systems: a RIEGL RiCOPTER equipped with a VUX-1UAV scanner (RIEGL LMS GmbH, Horn, Austria) and a DJI Matrice 600 Pro (DJI, Shenzhen, China) equipped with a YellowScan VX20 scanner (YellowScan, Saint-Clément-de-Rivière, France) based on the RIEGL miniVUX-1UAV (Table 1). Both systems have comparable laser ranging accuracy when considering large objects like trees, but the VUX-1UAV and miniVUX-1UAV operate at 1550 nm and 905 nm, respectively. Leaves and wood have very different reflectance properties at these two wavelengths due to stronger absorption of irradiance by water in the shortwave infrared (SWIR), which could influence target detection probability and hence the contribution of leaves and wood to the respective point clouds (Fig. 2). Additionally, the VUX-1UAV and miniVUX-1UAV have different laser footprints and ranging capabilities. The PRR of the VUX-1UAV can be tuned between 50 kHz to 550 kHz. The primary use of this feature is to increase the laser range by increasing laser power at the cost of PRR, allowing for higher altitudes to be flown. In this study this feature was exploited to vary the laser power: lower PRR results in higher pulse energy with each emitted pulse.

For this study, UAV-LS data were collected at the NE corner of Paracou's plot 6 between 10–21 October 2019. Different flight configurations were used: four flights following the same flight planning but for the VUX-1UAV with varying PRR of 100 kHz, 300 kHz and 550 kHz described as high power (HP), medium power (MP) and low power (LP) settings in the following, respectively, and for the miniVUX-1UAV with fixed PRR of 100 kHz described as YellowScan power (YS) (Fig. 5b). Additionally, four flights with the VUX-1UAV following the four cardinal directions with fixed PRR of 550 kHz (Fig. 5d) were undertaken. All VUX-1UAV and YellowScan miniVUX-1UAV flights were conducted at 6 m s^{-1} and 5 m s^{-1}, respectively.

All collected raw data underwent processing with standard tools. For VUX-1UAV data, this included processing recorded global navigation satellite system (GNSS) and base station data to flight trajectories with POSPac Mobile Mapping Suite 8.3 (Applanix, Richmond Hill, Ontario, Canada), laser waveform processing to discrete returns and geolocation in world coordinates with RIEGL RiProcess 1.8.6. For miniVUX-1UAV, waveform processing is performed online in the sensor. Point cloud processing and geolocation was performed with the CloudStation software (Yellowscan, Montpellier, France), using the Strip Adjustment option. For all UAV-LS data, only points with a reflectance larger than −20 dB were kept for further processing. Points with reflectance smaller than −20 dB consist mainly of spurious points caused by water droplets under high humidity conditions (Schneider et al., 2019).

2.3. Canopy volume occlusion

The point clouds were subsampled according to the scanner and flight experiments (Section 2.4) and processed to assess canopy occlusion (Fig. 3). Occlusion has the advantage that it measures the ability of the LiDAR to penetrate a canopy, which is relevant for estimation of canopy properties (Schneider et al., 2019; Pimont et al., 2018). In contrast to simple point cloud statistics like height percentiles, occlusion mapping takes into account the travelled distance of the laser pulses through the canopy and thereby accounts for empty canopy volume. Occlusion in general was defined as the hampering of return detection caused by objects in the path of LiDAR pulses. An occluded

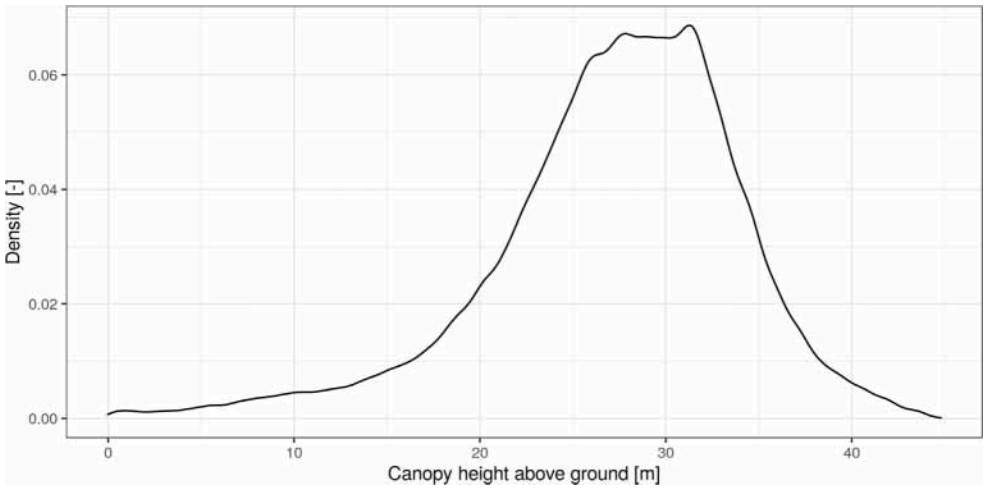

Fig. 1. Distribution of canopy heights across heights in the study area.

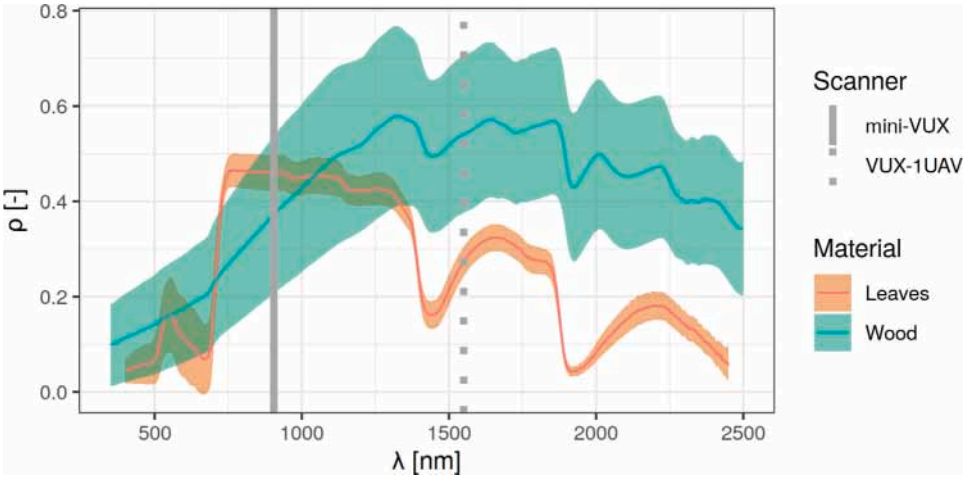

Fig. 2. Spectral reflectance factors ρ of different vegetation materials relevant for forest canopies at the 905 nm (miniVUX-1UAV) and 1550 nm (VUX-1UAV). Solid lines represent average ρ and ribbons ±1 standard deviation. Wood material summarises bark and branch data extracted from the ECOSTRESS Spectral Library (v1.0, https://speclib.jpl.nasa.gov/, Baldridge et al. 2009, Meerdink et al. 2019), leaf data from the Angers database (http://opticleaf.ipgp.fr/index.php?page=database, Féret et al. 2008, 2017).

Table 1
RIEGL VUX-1UAV and miniVUX-1UAV characteristics, including three scan programmes of the VUX-1UAV used in this study (RIEGL LMS GmbH 2021b, 2022, RIEGL laser classification sheets for pulse properties).

Characteristic	VUX-1UAV			miniVUX-1UAV
Maximum effective measurement rate [kHz]	500			100
FOV [°]	330			360
Ranging accuracy & precision [mm]	10 & 5			15 & 10
Laser wavelength [nm]	1550			905
Beam divergence [mrad]	0.5			1.6 × 0.5
Pulse width [ns]	3			6
Range resolution [m][a]	0.45			0.90
Weight (with cooling fan) [kg]	3.75			1.6
Scan power scenario	HP	MP	LP	YS
PRR [kHz]	100	300	550	100
Pulse energy [nJ]	5380	–	–	116
Maximum range $\rho \geq 0.2$ [m]	400	230	170	170
Maximum range $\rho \geq 0.6$ [m]	660	400	300	290
Maximum range $\rho \geq 0.8$ [m]	760	450	340	350

[a]According to Wagner et al. (2006).

voxel was defined as a voxel that lay on the pulse trajectory of one or multiple fired pulses, but beyond the last return of all these pulses when seen from the scanner. It could also not be visited by a pulse fired from another part of the flight trajectory. This means that any voxel visited by one or multiple pulses was not regarded as occluded.

Additionally, the principal mechanisms that caused occlusion were classified *a priori*. Absolute, geometrical and turbid occlusion were distinguished (Fig. 4). Absolute occlusion was defined as the complete optical obstruction of canopy volume against LiDAR exploration. This would be the case for example in the inside of a trunk. This would

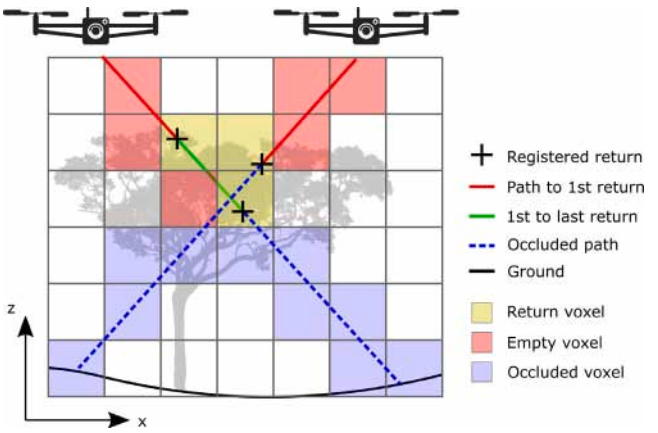

Fig. 3. Concept of occlusion with multiple return, multiple view point LiDAR. Tree silhouette by Johnson (2021). UAV designed by Freepik.

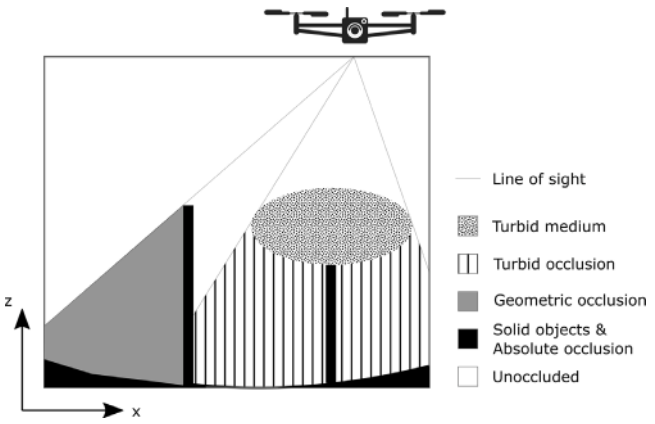

Fig. 4. Locations of different occlusion types introduced in this study. UAV designed by Freepik.

be the minimum level of occlusion to be expected from any scene, independent of the deployed LiDAR scanner and flight plan. In fact, characterising the absolute occluded volume is another way to express the main task of LiDAR vegetation surveys, which is quantifying biomass and foliage.

Geometric occlusion referred to a macroscopic, directional blocking effect, which could be overcome if the volume was observed from another direction, e.g., with additional flight lines or from below the canopy. Geometric occlusion implies that obstructing objects are larger than the effective laser footprint.

Finally, turbid occlusion was defined as the occlusion of the laser pulse due to interactions with targets smaller than the effective laser footprint. This occlusion is affected by the laser's properties, including wavelength, pulse shape, and waveform processing, and target properties, including size, orientation and reflectance at the scanner's operating wavelength. Another LiDAR scanner with different properties like increased power or operation at another wavelength could overcome this occlusion effect. Additionally, measures that reduce geometrical occlusion can also mitigate turbid occlusion. The term turbid was loaned from passive optical sensing where turbid media refer to volumes occupied by infinitesimal scatterers.

A special case of turbid occlusion is the scanner's range resolution in the case of multi-return capable systems. Specifically, returns cannot be distinguished from each other if they are too close to each other. The range resolution can be calculated as $v\tau/2$, where v is the speed of light and τ is the LiDAR's pulse width (Wagner et al., 2006). A typical forest consists of small and large targets, so that all these occlusion effects occur within the same scene.

A voxel traversal routine was implemented to identify voxels that were hit, empty or occluded Appendix. For occlusion mapping, cubic voxels with 10 cm side length were used. This side length is in line with Schneider et al. (2019), who worked with similar UAV-LS data. The side length is a compromise between four factors: first, the effective laser footprint, which is roughly 5 cm based on a flight altitude of 100 m for the VUX-1UAV. Second, the co-registration error between flight lines. Third, voxel size needed to be large enough for meaningful analysis of canopy and tree metrics. For example, estimation of crown parameters like volume would be meaningful at 10 cm side length, but much larger side lengths would introduce errors due to canopy discretisation into voxels. Fourth, computation time, which would exponentially increase with smaller voxels.

After voxel traversal, all voxels were height-normalised by subtracting the ground height based on a digital elevation model (DEM). This allowed to summarise voxels based on their height above ground and analyse effects in relative heights. The DEM was produced with all available point clouds and using lastools (Rapidlasso GmbH, Gilching, Germany) at 10 cm resolution. Therefore, all heights are above ground level if not specifically mentioned otherwise.

2.4. Scanner and flight experiments

The guiding principle for the experiments was that of fair comparison. The main goal was to limit the effects of scan settings. In practice, this meant that the number of fired pulses between scenarios should remain comparable. Additionally, observations were aggregated over areas as large as possible, which increased the number of sampled pulses. This reduced random effects like deviations of trajectories when flying the same flight plan multiple times.

2.4.1. Pulse repetition rate

The goal of this experiment was to investigate the effect of reduction in PRR applied to the same observed canopy volumes and with constant laser properties. PRR varies strongly between UAV-LS systems and a primary specification to look for when acquiring new systems. For this experiment, all 11 flight lines in NE direction were used with a rectangular AOI that covered the whole study area (Fig. 5a). The VUX-1UAV point clouds were acquired with the 550 kHz PRR scan programme and were subsampled to simulate different effective PRRs (Fig. 6). The subsampling of the 550 kHz point cloud produced synthetic point clouds as if they were produced by systems with different PRRs but the same trajectories and laser properties, thereby sampling the same vegetation volumes. It should be noted that the actual PRR of the scan programmes were not changed in this experiment, as opposed to the pulse power experiment (Section 2.4.2) and that the PRR changes were simulated using subsampling. For each subsampled point cloud, one pulse out of n was selected from the 550 kHz point cloud with $n = 2, 3, \ldots, 15$ to simulate PRRs ranging between 36.7 kHz and 275.5 kHz. The single pulses were identified by the GPS time registration attribute. It should be noted that both VUX-1UAV and mini-VUX have rotating mirror scanners that are mounted perpendicular to the flight direction. This means that the nominal PRR is given for 360° field of view (FOV). Hence, the effective PRR for a given FOV of interest is only a fraction of the nominal PRR given for 360° (e.g., PRR for a FOV of 90° is nominal PRR divided by four).

The PRR is a basic property of a LiDAR sensor that has strong impact on produced point cloud densities and hence productivity. A higher PRR allows denser point clouds, or faster flying and thereby larger coverage. UAV-LS systems have evolved from PRR of 12.5 Hz (for simultaneous coverage across the FOV of 110°) of custom-built solutions (Jaakkola et al., 2010; Wallace et al., 2012) to 1800 kHz of recent high-end UAV-LS scanners (RIEGL LMS GmbH, 2021a). A higher PRR allows to reduce geometric occlusion through increased use of gaps that would have been missed with a lower PRR, leading to more exploration of lower canopy layers.

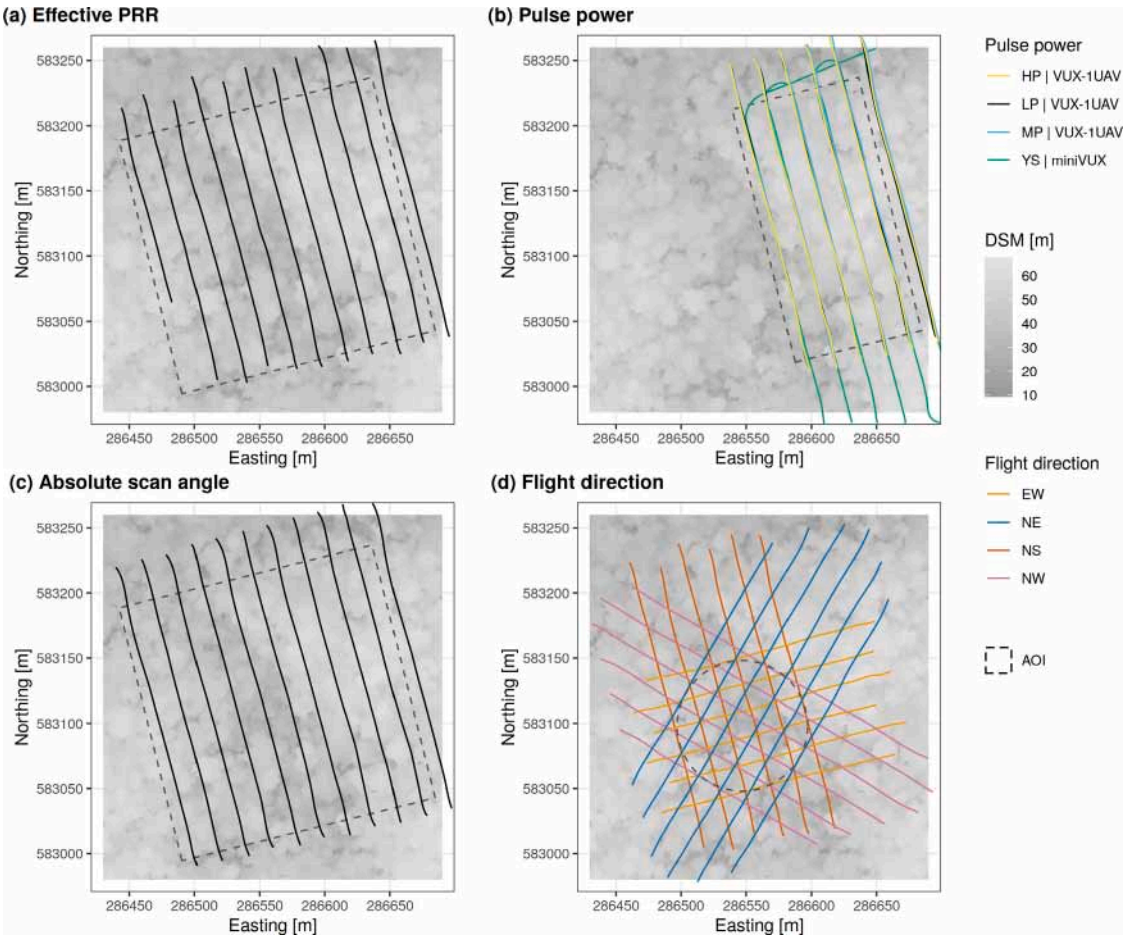

Fig. 5. Flight trajectories and AOIs for the flight experiments: (a) effective PRR, (b) pulse power and wavelength, including area for transect over pulse power scenarios, (c) absolute scan angle, (d) flight direction. Power modes refer to PRR and are high power (HP) (100 kHz), medium power (MP) (300 kHz), low power (LP) (550 kHz), YellowScan power (YS) (100 kHz) modes. Coordinate reference system is UTM22N with vertical datum of French Guiana. DSM heights refer to absolute heights.

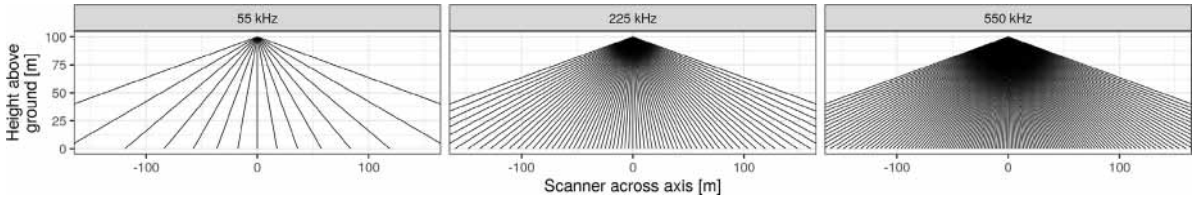

Fig. 6. Schematic overview for subsampling of point clouds to achieve different PRR.

2.4.2. Pulse properties

The pulse properties pulse power, wavelength and shape were investigated in this experiment. In order to examine the effects of laser pulse power on canopy occlusion, the tuning capability of the VUX-1UAV was exploited (Section 2.2). Three flights with different power levels were performed with the same flight paths and AOIs (Fig. 5b), but different scanning programmes with PRR of 550 kHz, 300 kHz and 100 kHz designated as low (LP), medium (MP), and high power (HP), respectively. In order to keep the absolute number of pulses fired of the 550 kHz and 300 kHz point clouds comparable to the 100 kHz point cloud, pulses were subsampled from the 550 kHz and 300 kHz point clouds. From the 550 kHz point cloud, every 1st and 6th pulse in a sequence of 11 pulses was selected. From the 300 kHz point cloud, every 1st pulse in a sequence of 3 pulses was selected (Fig. 7). As a result, resampled data sets had an effective PRR of 100 kHz.

Additionally, the miniVUX-1UAV was operated at the same PRR of 100 kHz as the HP level, but this scanner has a laser that operates at 905 nm (Table 1), allowing an assessment of the effect of the wavelength. However, it should be noted that the miniVUX-1UAV also has a different pulse shape and length, and lower pulse power than the VUX-1UAV, which might have an impact on results. The YellowScan miniVUX-1UAV results were labelled as YellowScan power (YS). It should be noted that the flight speed of the miniVUX-1UAV was slower compared to the VUX-1UAV (Section 2.2), resulting in higher number of pulses per unit area. Therefore, every 5th pulse was discarded from the YS point clouds.

Furthermore, for each of these settings the effects of recording only the first (FR) versus multiple returns (MR) from a laser pulse were investigated. Finally, the contribution of the different return orders to the respective power mode point clouds was investigated. For this, the return order of all returns of each power mode was extracted.

The pulse power is closely linked to PRR, but rarely specified by manufacturers. In fact, the PRR is inversely proportional to the laser pulse power for a given scanner. However, the maximum laser range can be regarded as a proxy for the laser power when reflectance

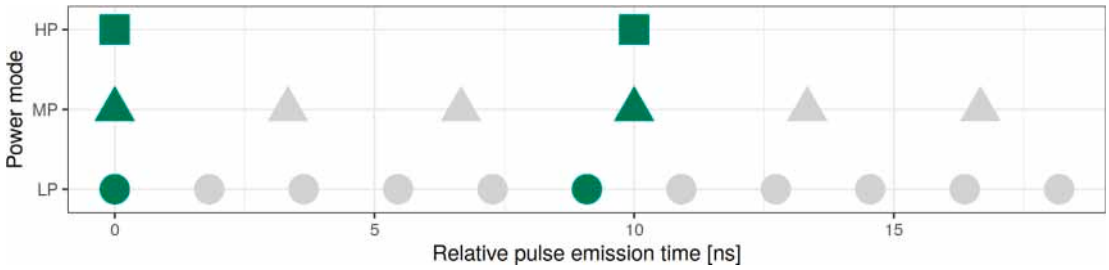

Fig. 7. Schematic overview for subsampling of point clouds depending on their pulse emission time to produce equal point cloud size for different power levels. Green indicates the selected pulses from each point cloud.

properties remain constant. On-board a UAV, power supply is limited by battery capacity and the availability of heat sinks for laser heat dissipation, which are in turn restricted by weight. This leads to a limitation on laser power and PRR. In practice, the laser can be designed to have high power for longer ranges, or lower power for shorter ranges at higher PRR. The minimum power and range are dictated by the flying altitude under consideration of the FOV. However, this calculation works only for bare terrain but in forests the canopy is the principal limiting factor that shields the lower canopy and ground from detection. In terms of range and hence laser power, different scanners are commercially available with varying specifications. Additionally, scanners operate at different wavelengths depending on the implemented scanner technology.

2.4.3. Absolute scan angle

There is a variety of UAV-LS scanners with different scanning mechanisms and viewing geometries, leading to different viewing angles covered during data collection. Therefore, the effect of scanning under different viewing angles was investigated. Only the HP flight of the VUX-1UAV was used, but with a rectangular AOI to maximise the sampled canopy volume (Fig. 5c). The point clouds were stratified according to the absolute scanning angle (ASA) and binned in 5° intervals (Fig. 8). ASA was defined as the absolute value of the scan angle rank (SAR), which in turn is defined as the angle of a pulse relative to the platform including the roll angle of the platform ranging from −90° to 90° (American Society for Photogrammetry and Remote Sensing, 2019). For ASA, the downward orthogonal direction relative to the platform is 0°. The directions to the left and right of the platform are 90°. As the RiCOPTER is an octocopter system, it needs to tilt to produce forward momentum, which means that $ASA = 0°$ does not correspond to the nadir direction. For example, during the HP flight the platform was tilted on average 4.4° forward to maintain the flight speed of $6\,m\,s^{-1}$. first return (FR) and multi return (MR) were analysed separately, as done for the power scenarios (Section 2.4.2). For analysis, ASA were binned in 5° wide bins and compared to the nadir bin at 0°±2.5°. Bins are addressed by their central value, e.g., 0°, 5° and 10°.

A range of different viewing geometries are available on the market. Typical FOVs are for example, 70.4° × 77.2° (conical) of the Zenmuse L1 (based on Livox sensor), 46° (conical) of the RIEGL miniVUX-1DL, 360° (planar) of the RIEGL miniVUX-1UAV series, and 330° (planar) of the RIEGL VUX-1UAV. Generally, a wide FOV increases the mapping productivity, but inertial measurement unit (IMU) errors affect high off-nadir angles stronger due to typically longer ranges at these angles and lead to lower registration accuracy. Additionally, forest canopies shield the lower canopy layers differently at different viewing angles, depending on the spatial arrangement of vegetation elements. The scan angle affects the observed geometric occlusion of a canopy.

2.4.4. Azimuthal flight direction

For UAV-LS flight mission planning, typically parallel line patterns are chosen to cover the target area. Cross-line patterns can be added to increase canopy exploration but these can require longer flight times and make the planning more complicated, so that the benefits of added directions need to be known to justify their implementation. For this experiment, flights were performed with flightlines aligned with the four cardinal directions (Fig. 5d). A circular instead of a rectangular AOI was used to avoid favouring a particular flight direction. In order to achieve a fair comparison, i.e., similar number of pulses fired between the trials, the point clouds were subsampled (Fig. 9). This means the point clouds were split into 2 and 4 sets when joining flight lines of 2 and 4 cardinal directions, respectively. In this way scenarios with only one flight direction could be compared to scenarios involving 2 or 4 directions. In practice, the subsampling was achieved by considering every 2^{nd} and 4^{th} pulse for 2 and 4 directions, respectively. This subsampling produced multiple combinations of actual flights, which were all independently processed and then averaged.

In addition to selection of the UAV-LS system, several options can be chosen to optimise the flight planning for canopy exploration. A basic trade-off is to whether the planned flight lines should be flown slower to increase the density of fired pulses on the target volume, or instead to fly faster and add flight lines at different azimuth angles. The number of azimuthal flight directions has an impact on the observed geometric occlusion of a canopy.

3. Results

3.1. Pulse repetition rate

Fig. 10 shows the occlusion observed with different PRRs at selected layers over the study area. At 1 m height, occlusion was highest ranging from 79.1 % to 96.0 %. Occlusion decreased with increasing height and was generally lower than 3.7 % at 35 m, where only the highest tree tops could shield canopy volume from observation (Fig. 1).

At altitudes ≥30 m, occlusion converged to low levels <5 % with increasing PRR. In the middle canopy from 10 m to 25 m, a strong decrease in occlusion with PRR < 300 kHz could be observed compared to lower and higher canopy layers, while the downward occlusion trends flattened towards PRR of 550 kHz. This suggests that marginal gain in exploration decreases with increased PRR. At the lowest canopy layers ≤5 m, the trend was even more shallow but relatively constant across all sampled PRR. This could mean that overall occlusion can only be reduced to the amount of absolute occlusion with much higher PRR, but with very small marginal gain. In summary, observed occlusion seemed to be easier to overcome in the upper canopy, while lower canopy parts require considerably higher PRR.

3.2. Pulse properties

All implemented pulse power settings showed comparable patterns of occlusion with first occluded voxels starting with the highest trees at circa 40 m, steadily increasing occlusion through the middle canopy, and high occlusion of 91.7 % to 99.4 % at 1 m above ground (Fig. 11a). In MR mode, MP and LP settings produced 3.6 % and 6.0 % more occlusion than HP across the whole canopy, with largest differences of 6.0 % and 9.8 % in the middle canopy around 20 m, respectively (Fig. 11b). The

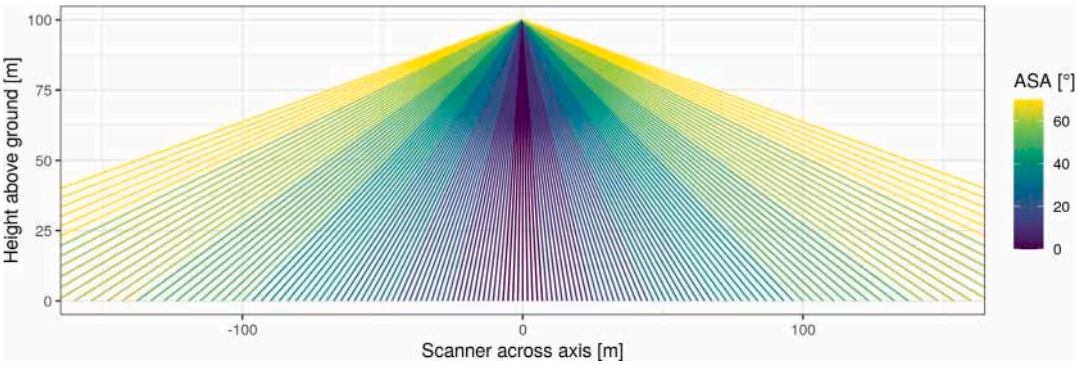

Fig. 8. Schematic overview for subsampling of point clouds depending on their ASA. Equal colours represent the strata used in the analysis.

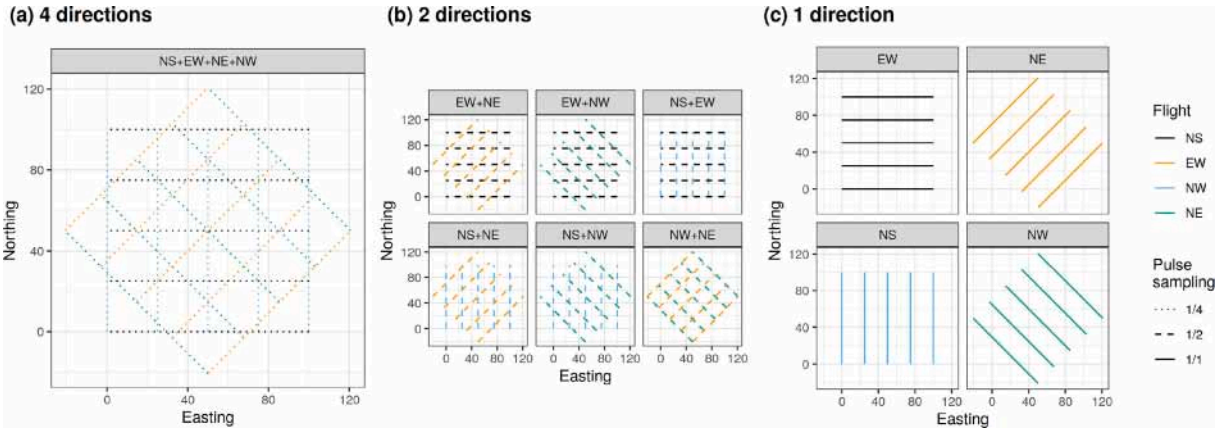

Fig. 9. Schematic overview for combination of point clouds in different directional configurations. Pulse sampling refers to the subsampling necessary to keep pulse numbers comparable between direction groups.

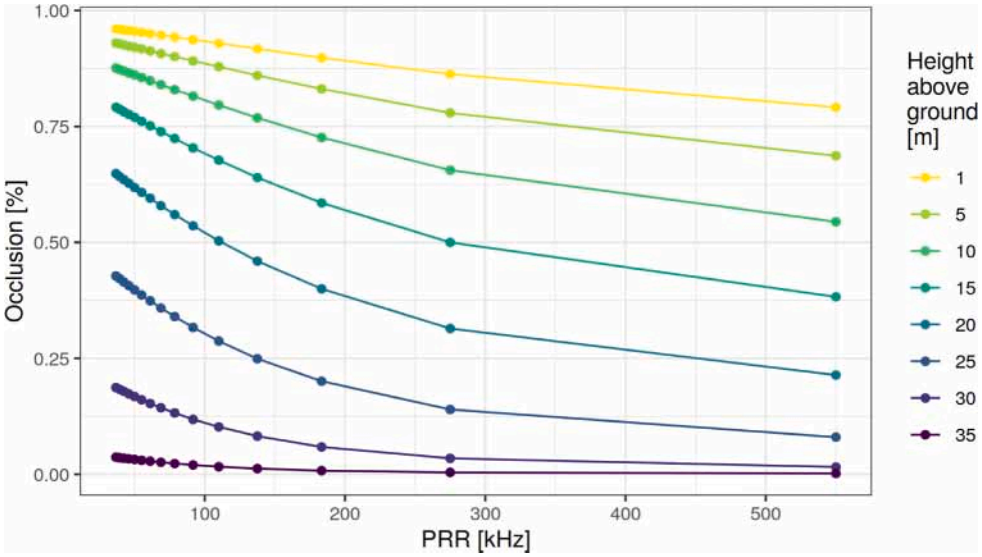

Fig. 10. Occlusion at different PRR and heights above ground level. PRR with respect to 360° FOV of the VUX-1UAV.

YS setting produced even more occlusion compared to HP of 7.8 % on average and with a maximum of 12.2 % at 20.4 m.

In FR mode, the ranking between the power modes remained the same as for MR, but the bulk differences between the power modes shifted from the middle to the upper part of the canopy (Fig. 11b). For example, the largest difference between HP and MP in MR was at 15.6 m, while it was at 26.4 m for FR. This can be explained by the generally higher levels of occlusion that occurred at lower canopy levels for FR. Overall, the MR mode was more strongly affected by reduced power than the FR mode.

The YS power mode experienced on average 7.8 % and 4.4 % more occlusion than HP mode for MR and FR modes, respectively, compared to 6.0 % and 1.8 % at LP mode. Differences to the LP mode reached up to 4.1 % of voxels and were most prominent in the upper canopy >15 m, while the lower canopy was characterised by a nearly constant offset in occlusion between YS and LP modes for MR.

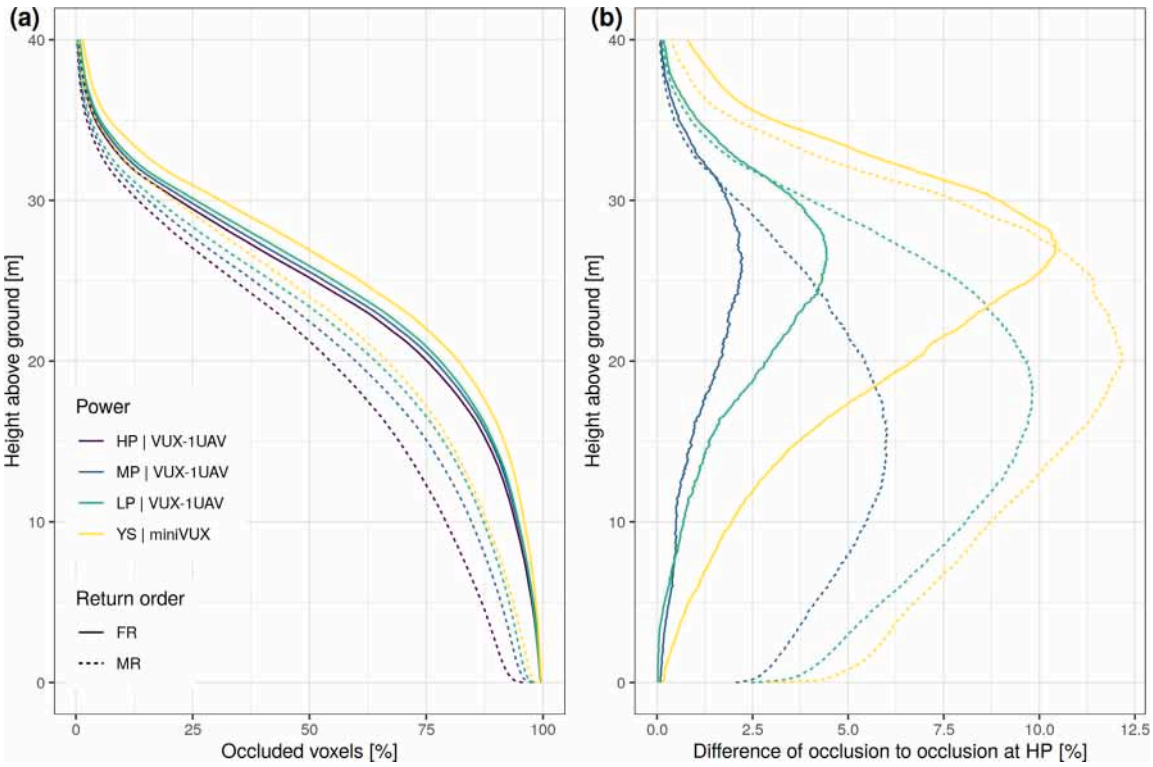

Fig. 11. Pulse properties' effects on occlusion relative to HP on canopy profile.

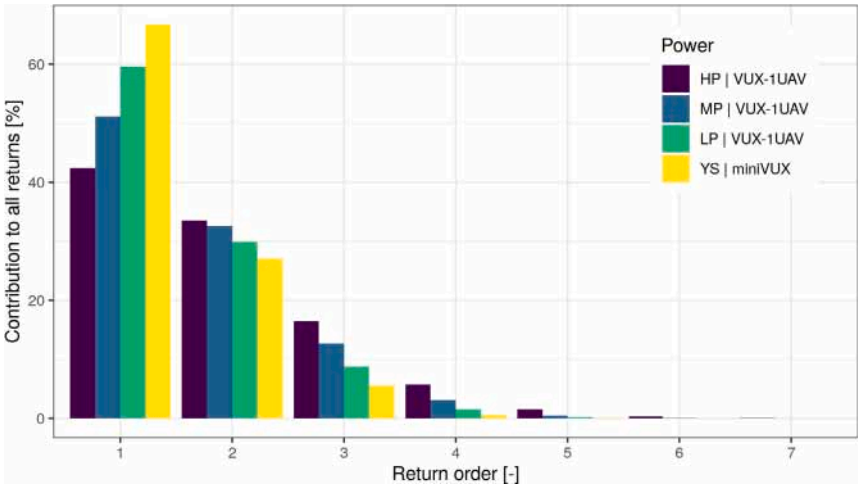

Fig. 12. Pulse properties' effect on return order.

3.3. Absolute scan angle

Fig. 13 summarises the occlusion effects of the observation angle expressed as ASA from 0° to 70° as the difference to ASA=0°. The largest differences with more than 30 % more occlusion could be observed from 20 m to 25 m. At heights above 30 m, which is higher than the average canopy (Fig. 1), differences were generally <5 %. An outlier was ASA=65° that produced less occlusion compared to ASA = 0°. This could be explained by better visibility of above canopy air space at larger angles and benefited from the ranging capacity of the VUX-1UAV of up to 760 m (Table 1).

The occlusion of larger ASA was larger for multi-return in the low canopy below 10 m, noticeable at ASA=65° with 3.6 % to 8.6 % difference in occlusion for first and multi-return, respectively. When summarised across the whole canopy, occlusion at ASA≤20° was slightly lower than at 0° with 0.2 % and 0.7 % difference in occlusion for first and multi-return, respectively (Fig. 14). For both return modes, occlusion increased nearly linearly until ASA=60°, then increased strongly. In summary, off-nadir viewing angles up to 20° experienced less occlusion in the middle to upper canopy.

3.4. Azimuthal flight direction

The setting using four directions produced 23.5 % average occlusion over the whole canopy, which was less occlusion than all other settings. This is why this setting was used as a reference for comparison (Fig. 15, Table 2). All single direction flights experienced more occlusion than any dual direction flight, with the single direction flight NE (at 26.2 % occlusion) being closest to dual direction flight NS+EW at 26.0 % occlusion. Overall, this highlights the importance to conduct flights in different directions to counteract occlusion.

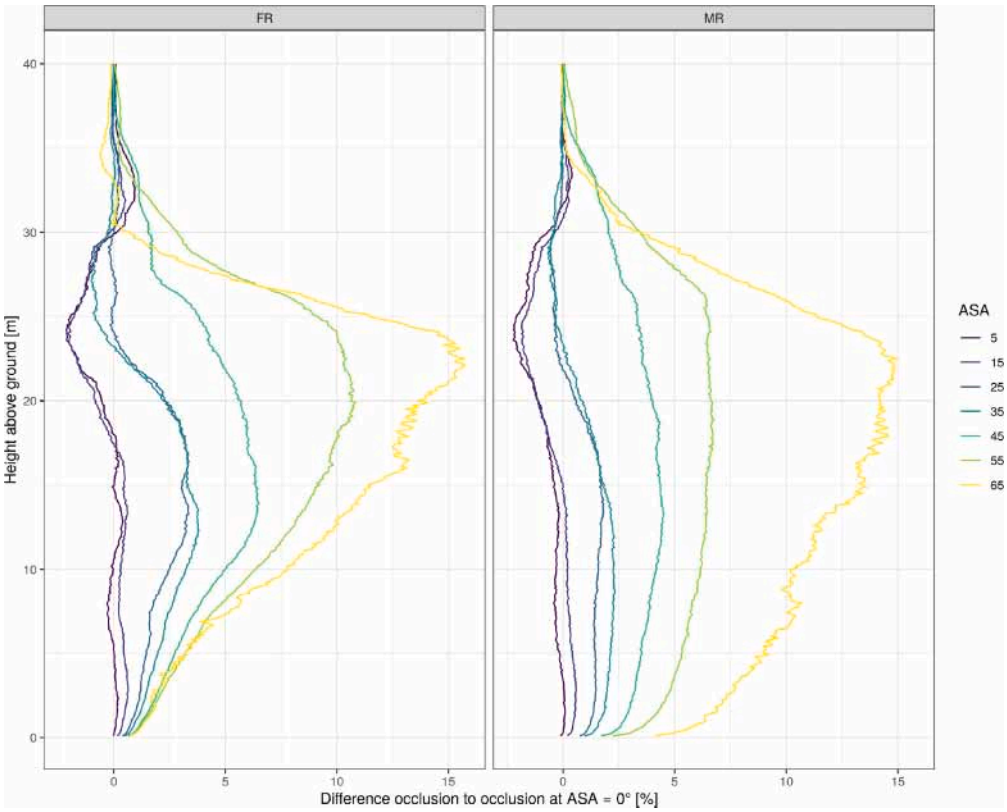

Fig. 13. Scan angle rank effect on occlusion relative to ASA=0° for FR and MR modes. Only every second bin up to 65° is displayed.

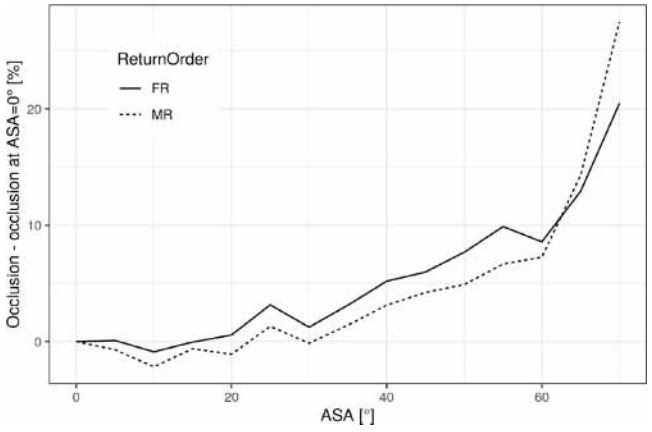

Fig. 14. Scan angle rank effect on occlusion across the canopy. The reference for the respective return modes FR and MR are the FR and MR settings at ASA=0°.

Fig. 15 displays how the individual flight directions compared to the four directions and to each other. The most pronounced differences in occlusion appeared in the middle canopy between 10 m and 15 m. The single direction flights produced different levels of occlusion with difference in occlusion compared to four directions of 2.8 %, 3.7 %, 4.2 % and 5.6 % for NE, EW, NW, NS directions, respectively. These differences propagated into the dual direction configurations. When used together, NW and NE produced the lowest occlusion, which was on the same level as the four direction setting. On the other hand, NS and NW resulted in 1.8 % more occlusion.

Table 2
Average flight direction effect on occlusion and difference to four directions.

Flights	Occlusion [%]	Occlusion - occlusion at four directions [%]
EW	27.2	3.7
NE	26.3	2.8
NS	29.1	5.6
NW	27.7	4.2
EW+NE	23.7	0.2
EW+NW	24.5	1.0
NS+NE	24.6	1.1
NS+NW	25.3	1.8
NS+EW	24.8	1.3
NW+NE	23.5	0.0
All	23.5	0.0

4. Discussion

In recent years, UAV-LS have evolved from custom-built prototypes to readily available survey-grade, turn-key solutions. With equally innovative applications comes the need for further standardisation and understanding of the capabilities and limitations of these systems. This study explored how scanner and flight planning properties affect the exploration of forest canopy volume based on experimental flights over a dense tropical forest. Most factors were found to influence the fraction of occluded canopy in the order of up to 10 % with highest impact in the upper canopy layers. These factors can potentially be optimised independently from each other.

4.1. Pulse repetition rate

In particular, UAV-LS systems have been made available with an increasing PRR over the past years. PRR is a key selling point for

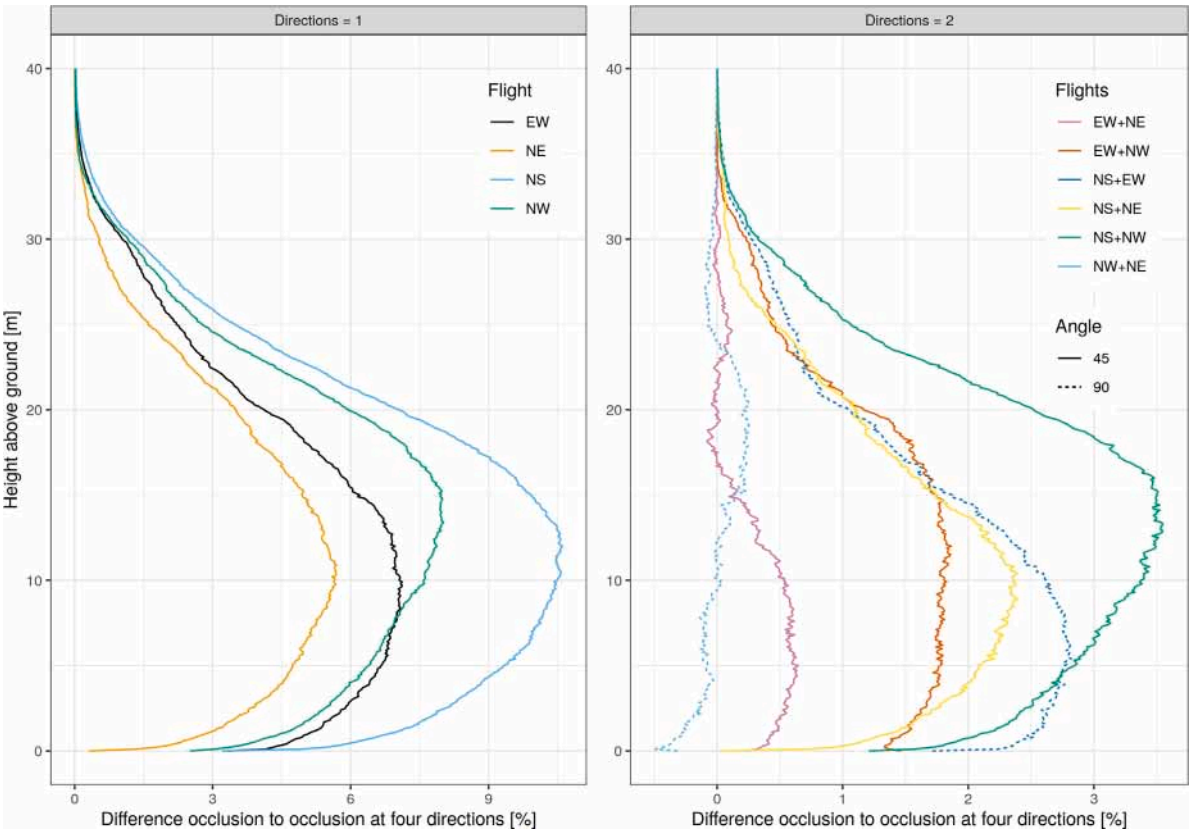

Fig. 15. Flight direction effect on occlusion.

UAV-LS sensors as it determines the point density and productivity. Typically, UAV-LS scanners nowadays have PRR of ≥200 kHz with the latest RIEGL VUX-120 having up to 1800 kHz (Hu et al., 2020). Results here suggest a saturation effect for middle and upper canopy layers beyond the 550 kHz for a scanner with properties as the scanners used in this study and at a flight speed of 6 m s^{-1}. This translates into approximately 100 kHz per 1 m s^{-1} flight speed. However, lower canopy layers might still benefit from higher PRR of latest systems. Additionally, flight mission boundaries should be regarded. For example, IMU accuracy deteriorates below a flight speed of approximately 4 m s^{-1} and fixed-wing systems have a stall speed below which insufficient lift is generated.

Considering different forest types, the level of required PRR can be expected to be lower for less dense and less complex forests such as temperate forests without understorey, savannas or even-aged plantations. On the other hand, higher PRR should be employed in particular for liana-infested tropical forests.

4.2. Pulse properties

The maximum measuring ranges of both miniVUX-1UAV and VUX-1UAV scanners exceeded the flight altitude and even included margins for off-nadir sampling (Table 1). Still, scanning programmes with higher maximum range and hence higher power were able to reduce occlusion, thereby exploring more canopy volume. Furthermore, the differences in occlusion between LP and MP were comparable to the differences between MP and HP. Even though these were only two power levels tested, this suggests that reduction in occlusion might still continue with higher power scanning programmes and longer range scanners (>760 m range, Table 1). Additionally, higher power modes could make better use of multi-return capabilities. This can be explained with higher initial energy of pulses that leads to higher remaining irradiance after interaction with first targets and higher irradiance at higher-order targets so that smaller fractions of beam coverage still triggered returns (Richter and Maas, 2022). A reduction in pulse power heavily affects the ability to detect partial hits. This could also be confirmed by the reduced contribution of higher order returns in the point clouds for lower pulse power (Fig. 12). The pulse power should also be considered when choosing a certain scan programme or scanner for a given flight speed. Extremely high PRR with only FR for a given flight speed might result in shallow returns from the top of canopy instead of entering the lower canopy layers.

Apart from power, scanner wavelength, beam divergence and pulse width also appeared to play a role in occlusion effects. As the range specifications between VUX-1UAV at 550 kHz (LP) and miniVUX-1UAV are similar (YS), the increased exploration of VUX-1UAV cannot be explained with the measured range and power alone, but was more likely related to different operating wavelengths, effective footprints and pulse shapes (Table 1, Fig. 2). For FR mode, a likely explanation for the observed differences in occlusion is the larger beam divergence and higher reflectance of foliage of the 905 nm miniVUX-1UAV (Fig. 2), which leads to returns being triggered higher up in the canopy and occlusion of the underlying canopy. For MR mode, an additional effect of the scanner's range resolution might have increased the difference even more. The miniVUX-1UAV range resolution was nearly twice as large as the VUX-1UAV (Table 1). In combination with a higher reflectance of leaves at the miniVUX-1UAV operating wavelength, this might have led to triggered returns at the very top of the canopy and no detected returns in the topmost canopy in this way. This effect is slowly dissipating with increased contribution of woody elements in the lower canopy <15 m. For MR mode on the other hand, higher order returns dominate in the lower canopy. Higher order returns stem from fragmented beam footprints, so that the original beam divergence and shape could play a smaller role and occlusion behaviour becomes more similar between YS and LP. Overall, miniVUX-1UAV could make less use of multi-return capacity because fewer photons travel on after first interaction with targets compared to the VUX-1UAV.

The two tested scanner wavelengths of 905 nm and 1550 nm are the two dominating wavelengths for UAV-LS. While 905 nm UAV-LS lasers use complementary metal–oxide–semiconductor (CMOS) technology based on gallium arsenide (GaAs) or aluminium gallium arsenide (AlGaAs) semiconductors, 1550 nm UAV-LS lasers are based on indium gallium arsenide phosphide (InGaAsP) semiconductors. One important difference is the easier availability of CMOS technology at lower costs, which led to the domination of UAV-LS by this type of scanners. Results here suggest that scanner wavelength, beam divergence and pulse width have effects on occlusion but detailed attribution in this study was limited because only two scanners were used. However, 1550 nm lasers with smaller beam divergence might have an advantage in the characterisation of wood and the lower canopy. On the other hand, combined use of multiple wavelengths can potentially be exploited for new applications like discrimination of leaf and wood returns (Shao et al., 2022).

The results obtained for the specific scanners used in this experiment can be expected to be generic with respect to their direction. Higher power lasers should result in registration of more higher order returns. Moreover, healthy vegetation typically follows the spectral signatures displayed in Fig. 2. Only under extreme drought conditions, higher reflectance at 1550 nm can be expected that leads to similar wood and foliage reflectances and consequently more similar responses of 905 nm and 1550 nm systems. Another extreme would be leaf-off conditions that result in only wood elements being present with more homogeneous spectral and geometric properties compared to a mixed wood-foliage canopy. Leaf-off conditions are generally favourable for canopy volume exploration but due to very different composition of the canopy it is difficult to predict how the different power and laser properties would affect occlusion.

4.3. Absolute scan angle

Concerning the optimal scan angles for minimal occlusion, slightly off-nadir angles seemed to be more suitable than nadir. This is in line with Brede et al. (2017) who found that ASA of 30° to 40° were optimal for trunk detection although results were species dependent. This window is still within the 40° window where occlusion was ≤5 % difference to ASA = 0° in this study (Fig. 14). Considering an optimal off-nadir scan angle of up to 20°, a lateral overlap of FOV of 50 % on the ground (Kükenbrink et al., 2017) and a flight altitude of 120 m, flight line spacing should be $tan\,20°\ 120\ m \approx 44\ m$.

For different sites with very different canopy conditions the optimal ASA might be different than the 40° found here even though a general trend should prevail. For example, very extreme foliage inclination angles would benefit or hamper canopy exploration at large angles. On the other hand, open canopies like savannas can be expected to profit from large angles because the volume below single standing trees' canopies is much easier to explore at large angles. However, it should be considered that large off-nadir require very long-range measurements and high accuracy IMUs.

An optimal off-nadir scan angle of up to 40° is at odds with Liu et al. (2018), who investigated scan angle effects on estimation of gap fraction with ALS data. Liu et al. (2018) recommended to avoid large off-nadir angles >23°. However, their recommendations are based on estimation methods that assume nadir view, which is compromising the estimation in heterogeneous stands with between-crown gaps. If the actual viewing angle is taken into account, angle effects should be addressed. As UAV-LS usually delivers higher off-nadir angles, viewing angles should be considered in methods development.

Based on these findings, it can be recommended to pay attention to the scanner FOV during acquisition of a new UAV-LS. Dedicated downward looking designs that provide sufficient off-nadir geometry should be preferred over designs that scan extreme angles. For example, the RIEGL VUX-1UAV has a 330° FOV and maximum PRR of 550 kHz. This results in an effective PRR of 150 kHz in the downward viewing direction assuming a FOV of 90°. Especially pulses in the upward direction are not useful but still emitted per design of the scanner. However, sub-optimal directions between 40° and 90° might still be useful for secondary roles like registration and trajectory optimisation tasks depending on mission characteristics.

4.4. Azimuthal flight direction

With respect to flight directions, it appeared that individual directions were affected differently and randomly. This should be expected in the absence of any major source of anisotropy in a natural stand as opposed to a plantation. Still, single directions were generally subjected to more occlusion than combinations of multiple directions. Whether the angle between the directions was either 90° or 45° did not make a difference. Next to reduced occlusion, multi-direction setups also have the advantage of providing cross-lines that connect different parts of the study area and increase co-registration quality (Brede et al., 2017). Hence, during flight planning at least two different directions should be considered. As an alternative to adding directions, the spacing between flight lines can be varied and thereby the overlap of flight strip products. For example, Kükenbrink et al. (2017) suggest an overlap of at least 50 %. As both miniVUX-1UAV and VUX-1UAV have a theoretical FOV of more than 180° this approach was not tested here. Nevertheless, addition of viewing angles into the canopy through flight directions or overlap can be expected to counteract occlusion.

4.5. Optimisation of flight protocol and scanner design

First of all, it should be mentioned that two important parameters of mission planning, namely flight speed and altitude were not explicitly covered in this study. However, flight speed is linked to the PRR in the way that doubling the flight speed would correspond to halving the PRR for a given travelled trajectory (Section 3.1). Flight altitude is directly affected by the scanner maximum range (Section 3.2).

Furthermore, different overall optimisation strategies could be pursued. This study aimed to give generic advice by investigating basic scanner properties, even though it was limited to dense canopies, which however should represent the most challenging conditions. The findings here could be the basis for specific advice for a given study area. This advice could be generated by acquiring data for a representative plot of a study area, analysing the scanner and planning parameters, and deriving specific recommendations for plots in the same area or with similar forest structure. A third approach could be an ad hoc adaptive approach that produces advice on trajectory optimisation during flights. For example, an ad hoc iterative approach was presented for TLS by Li et al. (2021). However, in the case of UAV-LS considerable technological advances need to be achieved for complex forest environments (Hyyppä et al., 2020).

Concerning generic optimisation of the scanning process, interactions between the examined parameters of this study could be further evaluated. This is also relevant because flight plans need to make compromises between parameters. For example, PRR and pulse power are inversely related for the RIEGL VUX-1UAV (Section 2.4.2). Additionally, different forest types and complexities would need to be considered. However, a comprehensive analysis of all interactions would quickly result in a very large number of experimental flights to be conducted.

A solution to produce a large number of experiments could be LiDAR numerical simulations that allow arbitrary flight protocols to be tested (Gastellu-Etchegorry et al., 2015; Winiwarter et al., 2022). In a first step, a representative virtual reconstruction needs to be created, which is not a trivial task (Calders et al., 2018). Then, in particular geometric parameters like PRR, ASA and flight directions can be easily implemented and tested. This would make geometric parameters easy to test with simulations.

Interactions of individual pulses with canopy elements smaller than the beam footprint as in the case of turbid occlusion are implemented as well. For example, HELIOS++ implements beam divergence and distribution of power within the beam via splitting the beam into subrays, which allows dealing with partial hits via waveform simulation and analysis (Winiwarter et al., 2022). However, modelling these interactions has limitations with respect to leaf properties like curled and irregular surfaces, or variation of reflectance properties within individual leaves. Also, modelling actual waveform analysis of commercial discrete return systems is problematic because these algorithms are closed source. For this purpose, calibration of models with observed data could overcome limitations to model interactions at the subfootprint level.

4.6. Occlusion mechanisms

When thinking of the different occlusion mechanisms (Section 2.3), it seems plausible that strategies that counteract geometric occlusion can compensate for each other. For example, a lower PRR could be compensated with additional flight lines, preferably in different directions. In this sense, PRR and additional flight directions are very helpful as they could produce considerable improvements (Sections 3.1 and 3.4). On the other hand, optimisation of ASA can involve the limitation to a certain maximum ASA. This could be beneficial if the fired pulses could be concentrated to these viewing angles, whereas filtering would simply discard pulses. An example here is the RIEGL miniVUX-3UAV that allows to limit the FOV and thereby increase the measurement rate for this window.

Turbid occlusion caused by pulse power and laser properties should be compensable with geometric strategies, at least to some degree. This is the case when canopy volume below dense sections can be explored from different directions, e.g., with additional flight lines. However, this might be limited in case of dense canopy parts with leaf area density $>5\,m^2\,m^{-3}$ (Soma et al., 2021). In these volumes partial hits dominate and make laser properties more important.

5. Conclusions & recommendations

In this study the effect of UAV-LS scanner and flight parameters on canopy occlusion were investigated with the aim to distil recommendations for the investment in UAV-LS scanners and campaign planning. The following conclusions based on the flights conducted can be drawn:

- PRR has a significant impact on occlusion. As a rule of thumb, at least 100 kHz per $1\,m\,s^{-1}$ flight speed for a scanner similar to the scanners used here should be chosen for the exploration of the middle strata (5 m to 20 m) of dense canopies, with relaxed requirements for open canopies. Higher PRR are beneficial for exploration of lower canopy (<5 m) but would need to be increased exponentially to achieve linear improvement. Alternatively, flight speed could be reduced at the cost of increasing flight time.
- The scanner maximum range specifications should not just be made dependent on flight altitude, but also on canopy complexity: dense canopies require higher power pulses and higher maximum range than flight altitude. In this study, no saturation effect with power could be observed and more powerful systems should be tested.
- Off-nadir scan angles of up to 20° (FOV = 40°) were comparable to nadir occlusion levels, with a slight decrease in occlusion at 10° to 20°. This optimal range would translate to a flight line spacing of 44 m at a flight height of 120 m and lateral overlap of FOV of 50 % on the ground.
- The exploration potential in particular directions over a given forest might be dependent on the discrete arrangement of individual crowns, which should be regarded as random in the mission planning stage. In order to ensure best exploration flying at best in four directions should be performed, while at least two directions are recommended.

All the investigated parameters were most effective to reduce occlusion in the middle and upper canopy. Occlusion at the bottom of the canopy cannot be easily overcome with UAV-LS alone due to combined geometric and turbid occlusion effects accumulating with increasing beam traversal length along with the limited power of UAV-LS systems. In this respect, canopy exploration would benefit from fusion with TLS data (e.g., Terryn et al. 2022), which adds very different observation geometries, thereby reducing geometric occlusion. Furthermore, a combination of LiDAR simulation and empirical experiments should be employed to test interactions between scanner and flight parameters with focus on interaction and compensation between parameters.

CRediT authorship contribution statement

Benjamin Brede: Conceptualization, Software, Methodology, Formal analysis, Data collection, Writing – original draft, Writing – review & editing, Project administration. **Harm M. Bartholomeus:** Conceptualization, Data collection, Writing – review & editing. **Nicolas Barbier:** Data collection, Formal analysis, Writing – review & editing, Funding acquisition. **François Pimont:** Methodology, Writing – review & editing. **Grégoire Vincent:** Conceptualization, Methodology, Writing – review & editing, Funding acquisition. **Martin Herold:** Funding acquisition.

Declaration of competing interest

The authors declare that they have no known competing financial interests or personal relationships that could have appeared to influence the work reported in this paper.

Data availability

Data will be made available on request.

Acknowledgements

This work was carried out as part of the Forestscan and QA4EO contracts funded by ESA-ESRIN. The study was carried out at Paracou research station managed by CIRAD-UMR EcoFoG (https://paracou.cirad.fr) and benefiting from funding from the Investissement d'Avenir grants of the ANR, France (CEBA: ANR-10-LABX-0025). Many thanks go to Leonardo Mauri for supporting the fieldwork and campaign in Paracou. The very constructive and thoughtful comments of two anonymous reviewers are gratefully acknowledged.

Appendix. Voxel traversal algorithm

First, the study area was divided into cuboids and the laser pulses were clipped according to the cuboids with the Cohen–Sutherland algorithm (Sproull and Newman, 1973). Subsequently, the cuboids could be processed independently and in parallel to speed up computations. Then, the traversal algorithm was applied on the cuboids and clipped pulses (Fig. A.16):

1. Define a 3D grid with resolution in x, y, z (corresponding to Easting, Northing, Height).
2. Define pulse trajectories based on flight trajectory as origin and hit coordinate as end point. Extend the pulse trajectories to the height of the lowest z grid coordinate.
3. Identify crossing points of pulse vector with grid c_n separately for each dimension.
4. Sort crossing points in x, y, z dimensions according to Euclidean distance to origin.
5. Define the path through a voxel p as the segment between consecutive crossing points c_n and c_{n+1}.

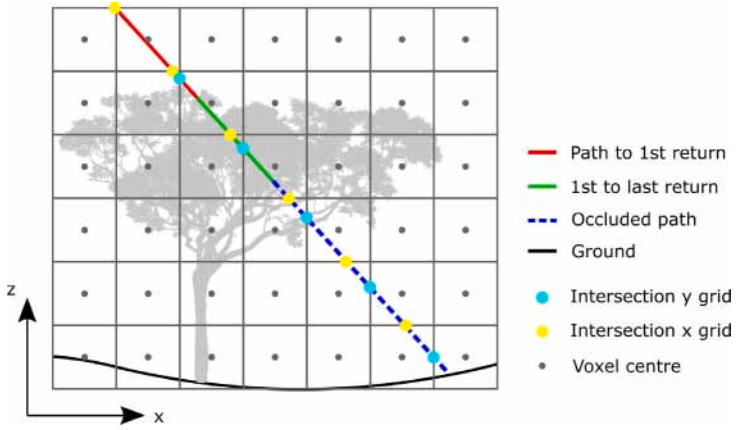

Fig. A.16. Graphical description of the voxel traversal algorithm.

6. Calculate mid-point of p as $(d_{entering} - d_{exit})/2$, where d refers to the three dimensions x, y, z. Derive nearest voxel centre coordinates as $round(d/res_d) * res_d$, where res_d is the resolution of the grid in dimension d.
7. Define crossed voxels as (1) empty if they do not contain a return and their exit point is closer to the scanner than the last return, (2) returns if the last return is between entry and exit point, (3) occluded if their entry point is further away from the scanner than the last return.

References

American Society for Photogrammetry and Remote Sensing, 2019. LAS Specification 1.4 - R15. https://www.asprs.org/wp-content/uploads/2019/07/LAS_1_4_r15.pdf.

Baldridge, A., Hook, S., Grove, C., Rivera, G., 2009. The ASTER spectral library version 2.0. Remote Sens. Environ. 113 (4), 711–715. http://dx.doi.org/10.1016/j.rse.2008.11.007, URL https://linkinghub.elsevier.com/retrieve/pii/S0034425708003441.

Brede, B., Calders, K., Lau, A., Raumonen, P., Bartholomeus, H.M., Herold, M., Kooistra, L., 2019. Non-destructive tree volume estimation through quantitative structure modelling: Comparing UAV laser scanning with terrestrial LIDAR. Remote Sens. Environ. 233 (January), 111355. http://dx.doi.org/10.1016/j.rse.2019.111355, URL https://linkinghub.elsevier.com/retrieve/pii/S0034425719303748.

Brede, B., Lau, A., Bartholomeus, H.M., Kooistra, L., 2017. Comparing RIEGL RiCOPTER UAV LiDAR Derived Canopy Height and DBH with Terrestrial LiDAR. Sensors 17 (10), 2371. http://dx.doi.org/10.3390/s17102371, URL http://www.mdpi.com/1424-8220/17/10/2371.

Brede, B., Terryn, L., Barbier, N., Bartholomeus, H.M., Bartolo, R., Calders, K., Derroire, G., Krishna Moorthy, S.M., Lau, A., Levick, S.R., Raumonen, P., Verbeeck, H., Wang, D., Whiteside, T., van der Zee, J., Herold, M., 2022. Non-destructive estimation of individual tree biomass: Allometric models, terrestrial and UAV laser scanning. Remote Sens. Environ. 280, 113180. http://dx.doi.org/10.1016/j.rse.2022.113180.

Calders, K., Origo, N., Burt, A., Disney, M., Nightingale, J., Raumonen, P., Åkerblom, M., Malhi, Y., Lewis, P., 2018. Realistic Forest Stand Reconstruction from Terrestrial LiDAR for Radiative Transfer Modelling. Remote Sens. 10 (6), 933. http://dx.doi.org/10.3390/RS10060933, URL http://www.mdpi.com/2072-4292/10/6/933.

Calders, K., Schenkels, T., Bartholomeus, H., Armston, J., Verbesselt, J., Herold, M., 2015. Monitoring spring phenology with high temporal resolution terrestrial LiDAR measurements. Agricult. Forest Meteorol. 203, 158–168. http://dx.doi.org/10.1016/j.agrformet.2015.01.009.

Féret, J.B., François, C., Asner, G.P., Gitelson, A.A., Martin, R.E., Bidel, L.P.R., Ustin, S.L., le Maire, G., Jacquemoud, S., 2008. PROSPECT-4 and 5: Advances in the leaf optical properties model separating photosynthetic pigments. Remote Sens. Environ. 112 (6), 3030–3043. http://dx.doi.org/10.1016/j.rse.2008.02.012.

Féret, J.B., Gitelson, A.A., Noble, S.D., Jacquemoud, S., 2017. PROSPECT-D: Towards modeling leaf optical properties through a complete lifecycle. Remote Sens. Environ. 193, 204–215. http://dx.doi.org/10.1016/j.rse.2017.03.004.

Gastellu-Etchegorry, J.P., Yin, T., Lauret, N., Cajgfinger, T., Gregoire, T., Grau, E., Féret, J.B., Lopes, M.l., Guilleux, J., Dedieu, G., Malenovsky, Z., Cook, B.D., Morton, D., Rubio, J., Durrieu, S., Cazanave, G., Martin, E., Ristorcelli, T., 2015. Discrete anisotropic radiative transfer (DART 5) for modeling airborne and satellite spectroradiometer and LIDAR acquisitions of natural and urban landscapes. Remote Sens. 7 (2), 1667–1701. http://dx.doi.org/10.3390/rs70201667.

Hu, T., Sun, X., Su, Y., Guan, H., Sun, Q., Kelly, M., Guo, Q., 2020. Development and Performance Evaluation of a Very Low-Cost UAV-Lidar System for Forestry Applications. Remote Sens. 13 (1), 77. http://dx.doi.org/10.3390/rs13010077.

Hyyppä, E., Hyyppä, J., Hakala, T., Kukko, A., Wulder, M.A., White, J.C., Pyörälä, J., Yu, X., Wang, Y., Virtanen, J.P., Pohjavirta, O., Liang, X., Holopainen, M., Kaartinen, H., 2020. Under-canopy UAV laser scanning for accurate forest field measurements. ISPRS J. Photogramm. Remote Sens. 164 (December 2019), 41–60. http://dx.doi.org/10.1016/j.isprsjprs.2020.03.021.

Jaakkola, A., Hyyppä, J., Kukko, A., Yu, X., Kaartinen, H., Lehtomäki, M., Lin, Y., 2010. A low-cost multi-sensoral mobile mapping system and its feasibility for tree measurements. ISPRS J. Photogramm. Remote Sens. 65 (6), 514–522. http://dx.doi.org/10.1016/j.isprsjprs.2010.08.002.

Johnson, G., 2021. Tree silhouette. https://pixabay.com/users/GDJ-1086657/?utm_source=link-attribution&utm_medium=referral&utm_campaign=image&utm_content=2069728.

Jupp, D.L.B., Culvenor, D.S., Lovell, J.L., Newnham, G.J., Strahler, A.H., Woodcock, C.E., 2009. Estimating forest LAI profiles and structural parameters using a ground-based laser called 'Echidna'. Tree Physiol. 29 (2), 171–181. http://dx.doi.org/10.1093/treephys/tpn022, URL http://www.ncbi.nlm.nih.gov/pubmed/19203942.

Kellner, J.R., Armston, J., Birrer, M., Cushman, K.C., Duncanson, L., Eck, C., Falleger, C., Imbach, B., Král, K., Krůček, M., Trochta, J., Vrška, T., Zgraggen, C., 2019. New Opportunities for Forest Remote Sensing Through Ultra-High-Density Drone Lidar. Surv. Geophys. (0123456789), http://dx.doi.org/10.1007/s10712-019-09529-9, URL http://link.springer.com/10.1007/s10712-019-09529-9.

Kükenbrink, D., Schneider, F.D., Leiterer, R., Schaepman, M.E., Morsdorf, F., 2017. Quantification of hidden canopy volume of airborne laser scanning data using a voxel traversal algorithm. Remote Sens. Environ. 194 (Special Issue of the SilviLaser 2015 Conference), 424–436. http://dx.doi.org/10.1016/j.rse.2016.10.023.

Levick, S.R., Whiteside, T., Loewensteiner, D.A., Rudge, M., Bartolo, R., 2021. Leveraging TLS as a Calibration and Validation Tool for MLS and ULS Mapping of Savanna Structure and Biomass at Landscape-Scales. Remote Sens. 13 (2), 257. http://dx.doi.org/10.3390/rs13020257, URL https://www.mdpi.com/2072-4292/13/2/257.

Li, L., Mu, X., Soma, M., Wan, P., Qi, J., Hu, R., Zhang, W., Tong, Y., Yan, G., 2021. An Iterative-Mode Scan Design of Terrestrial Laser Scanning in Forests for Minimizing Occlusion Effects. IEEE Trans. Geosci. Remote Sens. 59 (4), 3547–3566. http://dx.doi.org/10.1109/TGRS.2020.3018643.

Liu, J., Skidmore, A.K., Jones, S., Wang, T., Heurich, M., Zhu, X., Shi, Y., 2018. Large off-nadir scan angle of airborne LiDAR can severely affect the estimates of forest structure metrics. ISPRS J. Photogramm. Remote Sens. 136, 13–25. http://dx.doi.org/10.1016/j.isprsjprs.2017.12.004, URL https://www.sciencedirect.com/science/article/pii/S0924271617303726.

Mandlburger, G., Hollaus, M., Glira, P., Wieser, M., Riegl, U., Pfennigbauer, M., 2015. First examples from the RIEGL VUX-SYS for forestry applications. In: Proceedings of Silvilaser. La Grande Motte, France, pp. 105–107.

Meerdink, S.K., Hook, S.J., Roberts, D.A., Abbott, E.A., 2019. The ECOSTRESS spectral library version 1.0. Remote Sens. Environ. 230, 111196. http://dx.doi.org/10.1016/j.rse.2019.05.015, URL https://linkinghub.elsevier.com/retrieve/pii/S0034425719302081.

Pimont, F., Allard, D., Soma, M., Dupuy, J.L., 2018. Estimators and confidence intervals for plant area density at voxel scale with T-LiDAR. Remote Sens. Environ. 215 (June), 343–370. http://dx.doi.org/10.1016/j.rse.2018.06.024.

Richter, K., Maas, H.G., 2022. Radiometric enhancement of full-waveform airborne laser scanner data for volumetric representation in environmental applications. ISPRS J. Photogramm. Remote Sens. 183, 510–524. http://dx.doi.org/10.1016/j.isprsjprs.2021.10.021.

RIEGL LMS GmbH, 2021a. RIEGL VUX120. http://www.riegl.com/products/unmanned-scanning/riegl-vux-120/.

RIEGL LMS GmbH, 2021b. RIEGL VUX120 datasheet version 2021-09-14. http://www.riegl.com/uploads/tx_pxpriegldownloads/RIEGL_VUX-120_Datasheet_2021-09-14.pdf.

RIEGL LMS GmbH, 2022. RIEGL miniVUX-SYS datasheet version 2022-06-28. http://www.riegl.com/uploads/tx_pxpriegldownloads/RIEGL_miniVUX-SYS_Datasheet_2022-06-28_03.pdf.

Schneider, F.D., Kükenbrink, D., Schaepman, M.E., Schimel, D.S., Morsdorf, F., 2019. Quantifying 3D structure and occlusion in dense tropical and temperate forests using close-range LiDAR. Agricult. Forest Meteorol. 268 (January), 249–257. http://dx.doi.org/10.1016/j.agrformet.2019.01.033.

Shao, H., Cao, Z., Li, W., Chen, Y., Jiang, C., Hyyppa, J., Chen, J., Sun, L., 2022. Feasibility Study of Wood-Leaf Separation Based on Hyperspectral LiDAR Technology in Indoor Circumstances. IEEE J. Sel. Top. Appl. Earth Obs. Remote Sens. 15, 729–738. http://dx.doi.org/10.1109/JSTARS.2021.3134651.

Soma, M., Pimont, F., Dupuy, J.L., 2021. Sensitivity of voxel-based estimations of leaf area density with terrestrial LiDAR to vegetation structure and sampling limitations: A simulation experiment. Remote Sens. Environ. 257 (February), 112354. http://dx.doi.org/10.1016/j.rse.2021.112354.

Sproull, B., Newman, W.M., 1973. Principles of Interactive Computer Graphics. McGraw–Hill, New York, p. 252.

Terryn, L., Calders, K., Bartholomeus, H., Bartolo, R.E., Brede, B., D'hont, B., Disney, M., Herold, M., Lau, A., Shenkin, A., Whiteside, T.G., Wilkes, P., Verbeeck, H., 2022. Quantifying tropical forest structure through terrestrial and UAV laser scanning fusion in Australian rainforests. Remote Sens. Environ. 271, 112912. http://dx.doi.org/10.1016/j.rse.2022.112912, URL https://linkinghub.elsevier.com/retrieve/pii/S0034425722000268.

Vandendaele, B., Fournier, R.A., Vepakomma, U., Pelletier, G., Lejeune, P., Martin-Ducup, O., 2021. Estimation of Northern Hardwood Forest Inventory Attributes Using UAV Laser Scanning (ULS): Transferability of Laser Scanning Methods and Comparison of Automated Approaches at the Tree- and Stand-Level. Remote Sens. 13 (14), 2796. http://dx.doi.org/10.3390/rs13142796.

Wagner, W., Ullrich, A., Ducic, V., Melzer, T., Studnicka, N., 2006. Gaussian decomposition and calibration of a novel small-footprint full-waveform digitising airborne laser scanner. ISPRS J. Photogramm. Remote Sens. 60 (2), 100–112. http://dx.doi.org/10.1016/j.isprsjprs.2005.12.001.

Wallace, L., Lucieer, A., Watson, C.S., 2014a. Evaluating tree detection and segmentation routines on very high resolution UAV LiDAR data. IEEE Trans. Geosci. Remote Sens. 52 (12), 7619–7628. http://dx.doi.org/10.1109/TGRS.2014.2315649.

Wallace, L., Lucieer, A., Watson, C., Turner, D., 2012. Development of a UAV-LiDAR system with application to forest inventory. Remote Sens. 4 (6), 1519–1543. http://dx.doi.org/10.3390/rs4061519.

Wallace, L., Musk, R., Lucieer, A., 2014b. An assessment of the repeatability of automatic forest inventory metrics derived from UAV-borne laser scanning data. IEEE Trans. Geosci. Remote Sens. 52 (11), 7160–7169. http://dx.doi.org/10.1109/TGRS.2014.2308208.

Wieser, M., Mandlburger, G., Hollaus, M., Otepka, J., Glira, P., Id, N.P., 2017. A Case Study of UAS Borne Laser Scanning for Measurement of Tree Stem Diameter. Remote Sens. 9 (11), 1–11. http://dx.doi.org/10.3390/rs9111154.

Wilkes, P., Lau, A., Disney, M.I., Calders, K., Burt, A., Gonzalez de Tanago, J., Bartholomeus, H., Brede, B., Herold, M., 2017. Data Acquisition Considerations for Terrestrial Laser Scanning of Forest Plots. Remote Sens. Environ. 196, 140–153. http://dx.doi.org/10.1016/j.rse.2017.04.030.

Wilkes, P., Shenkin, A., Disney, M., Malhi, Y., Bentley, L.P., Vicari, M.B., 2021. Terrestrial laser scanning to reconstruct branch architecture from harvested branches. Methods Ecol. Evol. 12 (12), 2487–2500. http://dx.doi.org/10.1111/2041-210X.13709, URL https://onlinelibrary.wiley.com/doi/10.1111/2041-210X.13709.

Winiwarter, L., Esmorís Pena, A.M., Weiser, H., Anders, K., Martínez Sánchez, J., Searle, M., Höfle, B., 2022. Virtual laser scanning with HELIOS++: A novel take on ray tracing-based simulation of topographic full-waveform 3D laser scanning. Remote Sens. Environ. 269, http://dx.doi.org/10.1016/j.rse.2021.112772.